

PET Imaging of Neurofluids



Liangdong Zhou, PhD, Yi Li, PhD, MD, Mony J. de Leon, EdD*

KEYWORDS

- Positron emission tomography • ^{11}C -Butanol PET • Cerebrospinal fluid (CSF) • Interstitial fluid (ISF)
- CSF clearance • Alzheimer's disease • Kinetic modeling • Glymphatic function

KEY POINTS

- The use of dynamic PET and the radiotracer ^{11}C -Butanol for the quantification of cerebrospinal fluid (CSF) and interstitial fluid flow is introduced.
- PET estimated CSF clearance from brain, ventricle, and nasal turbinates, is reduced in aging, Alzheimer's, and in the presence of amyloid.
- An anatomic validation of PET as a dynamic CSF biomarker is proposed.

INTRODUCTION

Neurofluid Pathways in the Brain

Fluid homeostasis and hydrodynamics in the brain are critical for maintaining its structural and metabolic health.^{1,2} The term neurofluids, which refers to cerebrospinal fluid (CSF) and interstitial fluid (ISF), describes fluids that are largely derived from blood and to a lesser extent, from the brain itself.³ In summary, ventricular CSF is produced through blood filtration and modification at the choroid plexus. Driven largely by the pulsatile cardiac cycle,⁴ the CSF then flows through the cerebral ventricular system, communicating with subarachnoid spaces (SAS). These fluids enter arterial perivascular spaces (PVS) and are distributed throughout the central nerve system (CNS), moving into extracellular and extravascular spaces as ISF.⁵ The movement of these neurofluids facilitates molecular communication within the brain and adds in CSF and blood clearance, carrying away metabolic and protein waste.^{6,7}

Glymphatic System as a Pathway for Neurofluids

The recently termed glymphatic system refers to a newly recognized network of pathways in the brain that facilitates efficient fluid exchange between CSF and ISF through the astrocyte foot

located aquaporin-4 protein.^{8–10} Diurnal regulation of this function is appreciated, and sleep disruptions have been demonstrated to influence glymphatic function and brain health.^{11,12} Moreover, decreased glymphatic clearance has been reported in animal models of Alzheimer's disease (AD) and other brain disorders such as Parkinson's disease, traumatic brain injury, amyotrophic lateral sclerosis, possibly contributing to disease-specific protein accumulations.¹³ In AD, beta-amyloid (A β) plaques accumulate with increasing age and genetic risks,^{8,14–16} and in sporadic AD, even in the absence of excess protein production.¹⁷ Such observations underscore the importance of quantifying neurofluids and understanding their dynamic interactions. Recent imaging studies, including the MR imaging contributions found in this edition as well as our reports, have emphasized the potential of multimodal glymphatic clearance evaluations.^{18–25}

PET Technology

The most common application of the PET technique involves using a radiolabeled receptor ligand, typically introduced into the peripheral venous system. The tracer circulates to the arterial tree and reaches the target organ and binds to a specific site for duration sufficient to estimate radioactivity-based receptor occupancy. The

Department of Radiology, Brain Health Imaging Institute, Weill Cornell Medicine, 407 E 61st Street Feil-2, New York, NY 10065, USA

* Corresponding author.

E-mail address: mdl4001@med.cornell.edu

Neuroimag Clin N Am 35 (2025) 223–238

<https://doi.org/10.1016/j.nic.2024.12.001>

1052-5149/25/© 2024 Elsevier Inc. All rights are reserved, including those for text and data mining, AI training, and similar technologies.

Downloaded for Anonymous User (n/a) at Weill Cornell Medicine Samuel J Wood Library from ClinicalKey.com by Elsevier on April 17, 2025. For personal use only. No other uses without permission. Copyright ©2025. Elsevier Inc. All rights reserved.

Abbreviations

ASL	arterial spin labeling
AUC	area under curve
Aβ	beta-amyloid
BCSF	blood-CSF
ChP	choroid plexus
CNS	central nerve system
CSF	cerebrospinal fluid
DR	drain rate
ECS	extracellular space
Gd	Gadolinium
IR	influx ratio
ISF	interstitial fluid
LV	lateral ventricle
NFT	neurofibrillary tangle
NL	normal
PVS	perivascular spaces
SAS	subarachnoid spaces
TAC	time-activity curve

binding location is imaged using a dual photon coincidence camera, which records positron-electron annihilation events, marked by the release of 2 photons whose time of flight to the coincident detectors is included in the reconstruction process.²⁶ Historically, quantitative PET imaging positron emitters followed the autoradiographic ¹⁴C-deoxyglucose modeling approach by Sokolov²⁷ and gamma camera evolution.²⁸ Clinical PET studies began in the late 1970s with ¹⁸F-Fludeoxyglucose (¹⁸F-FDG)²⁹ and L-Dopa,³⁰ using 1 cm single-slice cameras with a 1.5 cm full-width at half-maximum resolution and 10-20 min count uptake periods.^{31–34} This technology has evolved to include hundreds of developed PET ligands, allowing for whole-brain and whole-body imaging at 2-4 mm spatial resolution with 2 to 10 second time sampling.^{35–37}

PET as a Molecular Imaging Method for Alzheimer’s Disease

PET has been pivotal in diagnosing AD by using various tracers to target distinct pathologic features.³⁸ The initial PET tracer used was ¹⁸F-FDG, and in collaboration with the Brookhaven National Lab, de Leon and colleagues first reported decreased glucose metabolism in AD in the context of limited ¹⁸F-FDG uptake reductions in normal aging brain.^{39,40} Subsequent longitudinal studies demonstrated progressive reduction in ¹⁸F-FDG PET in the hippocampal formation and helped identify normal aging individuals at risk for cognitive decline.⁴¹ However, translating these research observations into clinical practice relied on imaging anatomic patterns of hypometabolism.⁴² The increased availability of cyclotrons for PET radiotracer synthesis and improved camera

technology facilitated the development of diagnostic imaging based on reduced activity in the parietal and temporal lobes and hippocampus.^{43,44} These regional observations were further supported by postmortem studies showing extensive regional tau pathology and neuronal loss.^{45,46} This convergence of findings led to Food and Drug Administration (FDA) approval of FDG-PET for the differential diagnosis between AD and frontotemporal dementia.^{47,48}

Alzheimer’s Specific PET Tracers

A major advance was the introduction of AD-specific PET based molecular imaging techniques first demonstrated with 2-(1-{6-[(2-[fluorine-18]fluoroethyl)(methyl)amino]-2-naphthyl}-ethylidene) malononitrile (¹⁸F-FDDNP) capturing both amyloid plaques and neurofibrillary tangle (NFT),⁴⁹ and soon after Pittsburgh compound B (¹¹C-PiB) PET with greater molecular specificity for Aβ.^{50–52} Today several amyloid tracers are FDA approved including ¹⁸F-Florbetapir,¹⁶ ¹⁸F-Flutemetamol,⁵³ and ¹⁸F-Florbetaben,⁵⁴ to visualize Aβ plaques. Also, there is 1 FDA approved NFT or tau PET tracer (¹⁸F-Flortaucipir,⁵⁵ and additional tau tracers are in testing ¹⁸F-MK-6240,⁵⁶ and ¹⁸F-PI-2620,⁵⁷ and other tracers.)

PET Tracers for Other Binding Sites Implicated in Neurodegenerative Pathologies

Additionally, other PET radioligands have been developed that offer descriptive views of AD-related pathology. These include tracers for neuroinflammation, such as (1-[2-chlorophenyl]-N-methyl-N-[1-methyl-propyl]-3-isoquinoline carboxamide) (¹¹C-PK-11195) and N-((2-(methoxy-11C)-phenyl)methyl)-N-(6-phenoxy-3-pyridinyl)acetamide (¹¹C-PBR-28) for activated microglia,^{58,59} (2-(4,5-Dihydro-1H-imidazol-2-yl)-1-[11C]methyl-1H-indole / 2-(4,5-Dihydro-1H-imidazol-2-yl)-1-methyl-1H-indole) (¹¹C-BU-99008) for astrocytes,⁶⁰ an aquaporin PET tracer 2-nicotinamido-1,3,4-thiadiazole (¹⁸F-TGN-020),⁶¹ and an alpha-synuclein tracer ¹⁸F-ACI-12589.⁶² The reader is referred to more thorough reviews on AD diagnostic PET imaging.^{63–65} Overall, PET tracers have significantly improved the early AD diagnosis, expanded the in vivo pathology characterization, contributed to screening and evaluating subjects for therapeutic AD trials, and the longitudinal staging of AD progression.^{66,67}

Rationale PET Tracers for Cerebrospinal fluid/ Interstitial fluid Imaging

MR imaging has relied on both exogenous intrathecally administered Gadolinium (Gd), which takes hours to reach the brain from the lumbar spine and

sequences relying on endogenous contrast (water), but which are limited to capturing a few seconds of tracer mobility, Intrathecal Gd is well known as a high value MR contrast agent probing brain damage.⁶⁸ Experimentally it has been shown useful in mapping CSF pathways. Gd is a hydrophobic agent, and in normal brain it does not readily cross from CSF to brain or from CSF to blood⁶⁹; these barriers are referred to as the blood-brain-barrier and blood-CSF (BCSF) barriers. Thus, the Gd approach although useful for characterizing CSF anatomy and tissue integrity, is not ideal to capture kinetics of fluid exchanges across compartments. For the endogenous contrast MR imaging, sequences such as arterial spin labeling (ASL) are designed to capture brain blood perfusion by tagging the water in blood to introduce an endogenous contrast^{22,70}; the signal decays very fast at the rate $1/T_{1b}$, with T_{1b} the T_1 relaxation time of blood, making it difficult to infer information about the communication with the ISF.^{71–74}

Given these limitations, de Leon and colleagues proposed a role for PET imaging with the intravenous (IV) administration of freely diffusible, nonbinding, and rapidly clearing tracers labeled with relatively long half-lives (20–110 min) to track the transfer across brain compartments. At the time of this writing, PET, ASL, and Gd approaches have demonstrated value in characterizing aspects of CSF clearance; however there are no head-to-head comparisons available.

Aims of this Review

In this review, we will focus on emerging dynamic PET approaches to imaging neurofluids in AD and preclinical AD. We will review studies targeting CSF and ISF dynamics in regions known to be associated with CSF flow and presumably the glymphatic system. These exploratory imaging studies have begun to reveal quantitative regional relationships between neurofluid tracer clearance, the AD diagnosis, aging, and amyloid deposition.

DYNAMIC PET IMAGING OF NEUROFLUIDS

PET studies have employed 2 classes of radiotracers to examine neurofluids. In the first publications,^{75,76} ^{18}F -tau tracers were used to estimate ventricular CSF clearance. This class of tracer was selected by taking into consideration the limited brain density distributions of tau lesions in aging as compared with A β lesions, and therefore were considered to be less confounding (loss of signal to lesion uptake). In these early studies, 90 min dynamic tau PET data with (6-[(3- ^{18}F fluoro-2-hydroxy)propoxy]-2-(4-methylaminophenyl)quinoline) (^{11}C -THK-5117) and 1-(Fluoro- ^{18}F)-

3-((2-(6-(Methylamino)-3-Pyridinyl)-6-Quinolinyloxy) (^{18}F -THK-5351) were acquired and sampled the lateral ventricle (LV), and built slope and AUC based models to quantify the tracer influx and clearance through CSF compartments. Later an amyloid tracer was reported to estimate ventricular CSF clearance.²⁴ In the second class of study, ^{11}C -Butanol, a freely diffusible, lipophilic tracer with tissue permeability similar to water and a 20 min $1/2$ life that did not bind to brain or AD lesions was repurposed from a cerebral blood flow (CBF) agent to a CSF clearance biomarker by expanding observation time windows.⁷⁷ ^{11}C -Butanol studies enabled direct examination of CSF and brain when blood tracer concentrations were low and asymptotic.

PET Imaging of Neurofluids

In principle, with the intravenous (IV) injection of a bolus of a small molecular weight, freely diffusible, and lipophilic molecule, the anatomic fate of the label can be followed. It is well known that IV delivered tracers pass through the lung and heart to enter the brain via the arterial blood. This blood carrying the tracer irrigates the entire brain, a portion of which is converted to CSF, and ultimately all tracer activity is cleared (Fig. 1). As such, the PET camera is used to estimate an optimal temporal viewing window for both the influx and the rapidly diminishing tracer concentrations in arterial blood as contrasted with the slower and delayed time courses for tracer distribution and clearance in CSF, brain, and venous compartments. See Fig. 2 highlighting arterial and venous timing and Fig. 3 for ventricular tracer uptake and clearance.

Conventional PET Modeling

The PET community has applied multiple modeling approaches to examine tracer dynamics in the brain, which includes time-activity curve (TAC) based modeling,^{75,76} the graphic analysis (Logan plot,⁷⁸ Patlak plot^{79,80}), and compartmental kinetic PET modeling.⁸¹ These conventional models are mostly used for both tracer uptake and steady state blood flow, and have been developed to estimate the rates of metabolism, membrane permeability, blood flow, etc.^{81–83} However, there is no consensus for modeling tracer egress to estimate the CSF clearance in the brain. Recently, several novel models were proposed to evaluate the neurofluids movement in the brain using dynamic PET.^{24,25,75,76,84}

Emerging Modeling of Cerebrospinal Fluid Dynamic

Ventricular space as clearance target

The brain ventricular system includes left and right LVs, and third and fourth ventricles, which are all

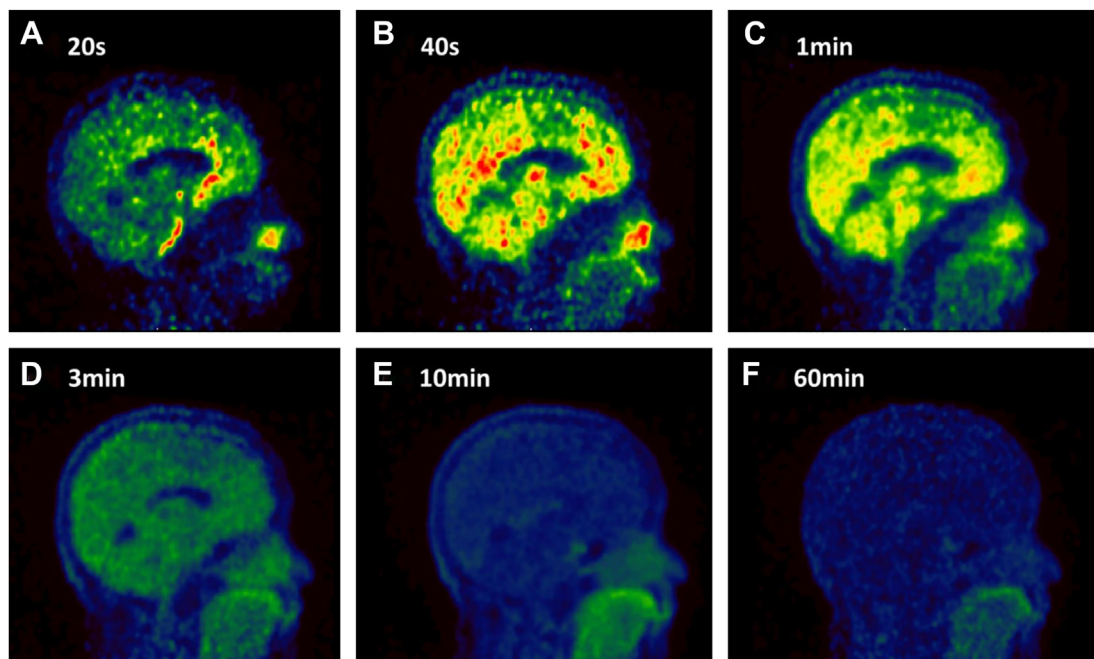


Fig. 1. Dynamic ¹¹C-Butanol PET image frames. Six frames from (A) to (F) are for 20s, 40s, 1 min, 3 min, 10 min, and 1 hour post IV tracer injection, respectively. The frames illustrate how the signal is enhanced and decreased in the brain depending on time. With the passage of time the tracer is cleared from the arterial vasculature, and it enters and mixes with other compartments, including the SAS, neural tissue and ISF, ChP, PV5, and drainage via lymphatic and venous outflow. (Source Mehta NH, Sherbansky J, Kamer AR, et al. The Brain-Nose Interface: A Potential Cerebrospinal Fluid Clearance Site in Humans. *Front Physiol.* 2022;12. <https://doi.org/10.3389/fphys.2021.769948>.)

filled with CSF. The choroid plexus (ChP) located in the ventricles, widely considered as the main source of CSF, is also recognized as a site absorbing a fraction of CSF.⁸⁵ Driven by cardiac based vascular pulsations and brain compliance,^{4,9} the ventricular CSF irrigates the brain and flushes metabolic waste from the ISF.⁸⁶ As the CSF pool in the LVs is the largest in the brain, it was selected in the early studies to investigate brain tracer clearance. In these nongated studies, (estimated) cardiac cycles of approximately 1 second were averaged over 10s to generate TAC using the relatively low spatial resolution (4 mm) PET imaging. Importantly, the PET tracers used had no LV ChP binding, providing an opportunity to map the CSF clearance using dynamic PET. **Fig. 3** shows an example of PET data TAC in LV and blood.

Extracranial cerebrospinal fluid clearance in relation to ventricular clearance

The use of dynamic PET to examine LV CSF clearance was first reported by de Leon and Li, and colleagues in 2017.⁷⁵ In that study, the tau PET tracer ¹⁸F-THK-5117 was used to estimate the CSF clearance by measuring the area under curve (AUC) between 35 and 80 minutes post tracer injection (AUC_{35-80min}). The 35–80 min interval was selected

to avoid contamination of the signal from blood, which was observed to reach asymptotic levels at about 4 min and to examine CSF clearance after any tracer binding to tau lesions was completed. This study reported that lateral ventricle CSF clearance for both the slope and the AUC_{35-80min} were reduced in AD ($P<.01$) compared with healthy normal (NL). When considering the rate of change of the ventricle, AUC normalized by the cerebellar AUC, the relative clearance was reduced by 33%, ($P<.01$) in AD. Further, the magnitude of the decreased LV CSF clearance demonstrated a strong relationship to an increased A β deposition as determined by ¹¹C-PiB PET ($\rho = 0.74$, $P<.05$).

In a replication of de Leon and colleagues' 2017 paper, Schubert and colleagues, 2019²⁴ examined CSF clearance in AD and control using ¹¹C-PiB PET with a 2-compartment model. They designed a PET kinetic model to quantify ventricular tracer clearance by including modeling compartments for gray matter, blood, and a ventricular bound pool. The results in this study were consistent with the prior vCSF work showing significantly decreased ventricular CSF clearance in AD as compared with NL.^{24,75,76}

While multiple non-human mammals studies have demonstrated a robust clearance pathway

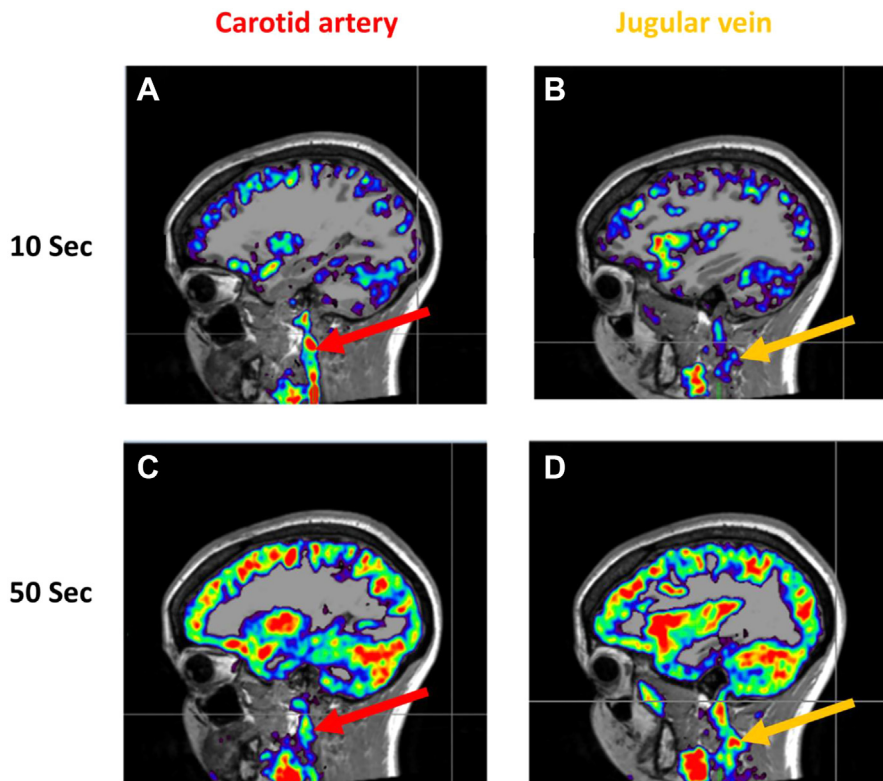


Fig. 2. An example showing the ^{11}C -Butanol PET signal enhancement in carotid artery and internal jugular vein by time. (A) shows at 10 seconds post tracer injection, the arterial signal (red arrow) and (B) the vein signal (orange arrow). At 10 seconds, the carotid artery is enhanced while there is no significant signal in internal jugular veins. (C) and (D) At 50 seconds post tracer injection, the arterial signal is decreased in (C) compared with (A) and the internal jugular vein signal (D) is increased as compared with (B). (Courtesy – de Leon MJ, Li Y, Zhou L.)

spanning from the subarachnoid space to cribriform plate and to nasal turbinates,^{87,88} this anatomy is poorly understood in human. The de Leon, and colleagues 2017 study also tested a suspected nasal turbinate CSF clearance route in human. Nasal turbinate clearance was reported and replicated using ^{11}C -cocaine PET. Of considerable interest, examination of the nasal tracer signals in the ^{18}F -THK-5117 study also showed an AD associated clearance reduction. **Fig. 4** shows the nasal and extracranial distribution of CSF correlated voxels. **Fig. 5** shows that all AD and control subjects have CSF-positive voxels in the superior turbinate which are reduced in AD. **Fig. 6** demonstrates the nasal turbinate signal using ^{11}C -cocaine PET data in healthy young subjects.

In a second LV CSF report from the same research team, Li and de Leon, and colleagues extended the numbers of impaired subjects and redefined the ventricular CSF clearance rate (vCSF) defined by the TAC slope between 10- and 30-min post injection divided by the whole brain AUC in the first 4 mins.⁷⁶ The normalization of TAC slope by the whole brain tracer input

improved the robustness of vCSF as a diagnostic tool.^{75,76} This revised definition of vCSF, normalizing for early blood flow effects and variations total tracer influx, provided a more robust estimation of CSF clearance as compared to the earlier metrics. **Fig. 7** shows the vCSF in association with amyloid lesions and in the classification of impaired subjects.

In a third set of studies from our group, Zhou, and colleagues 2023 developed a multimodal imaging assessment to characterize the CSF clearance anatomy.²⁰ These data showed that for A β positive subjects, a combination of the MR imaging based diffusion tensor image analysis along the perivascular spaces (DTI-ALPS) and ^{18}F -MK-6240 PET based vCSF improves the association with ^{11}C -PiB PET A β deposition ($P < .05$, $R^2 = 0.575$).²⁰ The combination is superior to either modality alone (vCSF: $P < .05$, $R^2 = 0.431$; ALPS: $P < .05$, $R^2 = 0.372$). Of considerable interest, this study also reported that PET vCSF ($n = 24$, $P < .05$, $r = -0.548$) is more sensitive than MR imaging DTI-ALPS. Overall, these observations, provided initial evidence that the description of the brain CSF clearance

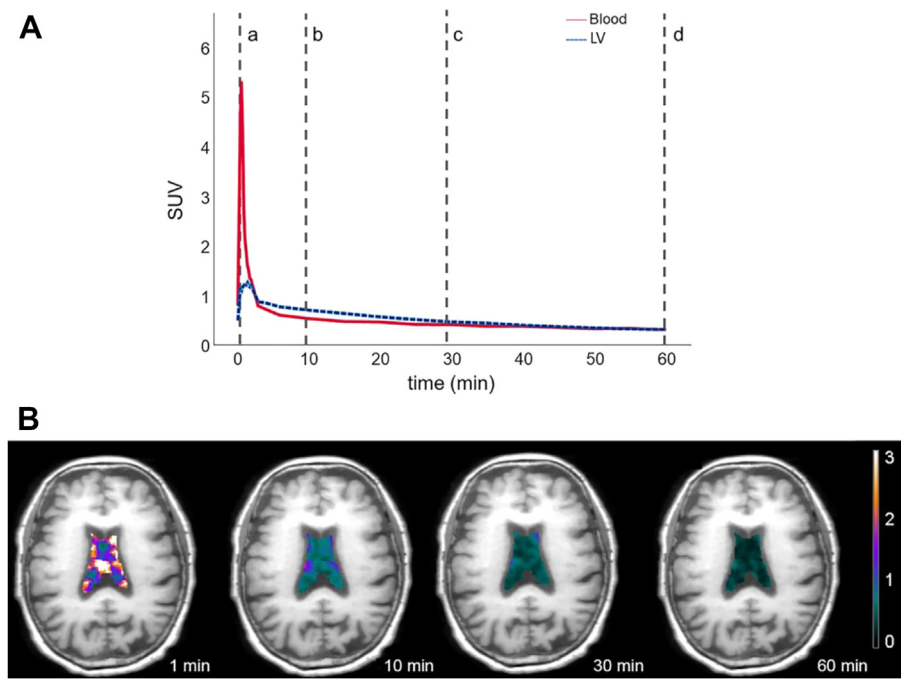


Fig. 3. An example of TAC of¹ 18F-THK5351 PET tracer in LV of human brain. (A) shows the TAC in both carotid artery and LV (B) shows the decreasing PET tracer concentration in LV from 1 min to 1 hour post injection. The ventricular tracer inflow is mainly driven by blood flow and choroid plexus function, while the ventricular tracer outflow is multifactorial, and includes: ventricular system flow, choroid plexus and venous drainage, and intracranial pressures. (Source Li Y, Rusinek H, Butler T, et al. Decreased CSF clearance and increased brain amyloid in Alzheimer's disease. *Fluids Barriers CNS*. 2022;19(1):21. <https://doi.org/10.1186/s12987-022-00318-y>.⁷⁶)

could be enhanced using both PET and MR imaging and thus a potential for multiple modality imaging of CSF dynamics in understanding the pathology of AD.

Butanol imaging of the nasal space as an extracranial cerebrospinal fluid pathway

While ¹¹C-Butanol was previously used as blood flow imaging agent,^{77,90,91} we repurposed the tracer to serve as a CSF/ISF biomarker.⁹² The idea behind the use of Butanol was to map without tissue binding, the temporal course of the tracer input and clearance from the carotid artery to the brain, ventricular, interstitial and cranial nerves, and ultimate passage to venous and jugular clearance. Butanol, with performance and permeability similar to labeled water ¹⁵O-H₂O, is also a tracer without a binding site.⁷⁷ However, because of its relatively long 20 min versus 2 min half-life, ¹¹C-Butanol enables improved compartmental imaging of tracer transit.^{77,90,93}

Unlike the ventricular CSF pool, a relatively homogeneous target for imaging, nasal CSF passes from brain via the cribriform plate along olfactory nerves to clear via venous and lymphatic vessels in a complicated nasal structure. Recently, Mehta and de Leon and colleagues, 2024 used ¹¹C-Butanol to examine the tracer clearance through

the brain and nasal anatomy.⁹² In this study, a new tracer clearance metric *t*75% was defined to estimate the time to clear 75% of tracer entering the region of interest between 0 to 60 min post tracer injection. A shorter *t*75% value indicates a faster speed for tracer clearance. It reported the *t*75% from the lateral orbitofrontal cortex (LOF) and an anatomic sample combining superior, middle, and inferior turbinates (All-turbinates) were positively and selectively associated, suggesting a connection between the brain and the nose. Further, the Aβ+ subgroup demonstrated impaired tracer kinetics in both regions, marked by reduced tracer influx (0–4 min) and slower egress (4–60 min) measured by *t*75%. The egress deficit is most readily seen in the nasal compartment (Fig. 8). It supported the interpretation that for the Aβ+ subgroup, impaired tracer egress from brain contributes in part to reduced turbinate tracer influx. It also raised the possibility that amyloid also impacts the tracer influx to brain.

Emerging Modeling of Extracellular Fluid Dynamic

Extracellular space structure

The extracellular space (ECS) refers to the space outside the cells that is filled with ISF containing

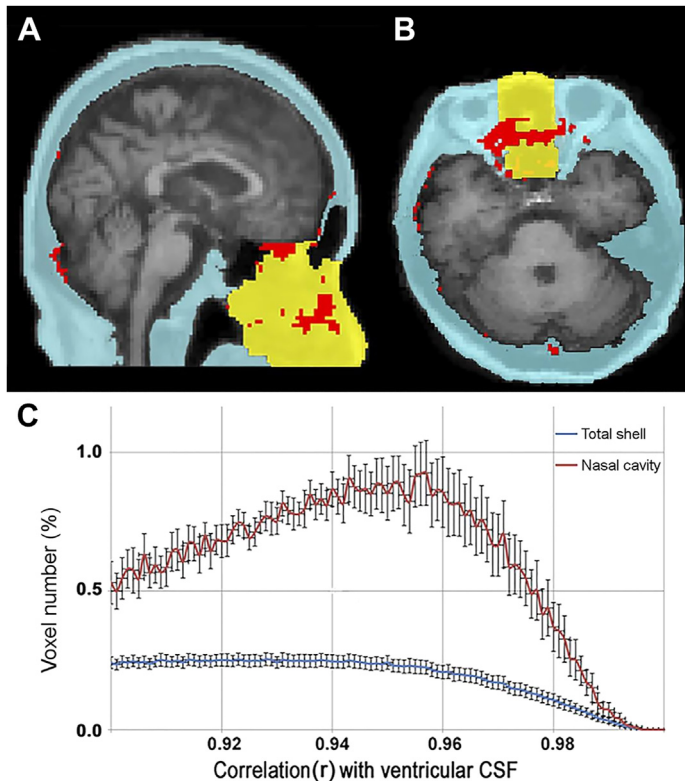


Fig. 4. Extracranial distribution of CSF TAC correlated voxels. Sagittal (A) and axial (B) MR images from a representative NL show 3-dimensional extracranial shell region in blue and total nasal cavity in yellow and red. (C) Percentage distribution (\pm SEM) ($n = 5$ subjects) of shell and nasal cavity voxels whose tau PET derived TAC are correlated with ventricular CSF TAC, within range of $r = 0.90$ to 0.99 , $n = 5$. Data show in red a 3-fold-greater percentage of CSF-correlated voxels in nasal cavity than in total shell. (This research was originally published in JNM. de Leon MJ, Li Y, Okamura N, et al. Cerebrospinal Fluid Clearance in Alzheimer Disease Measured with Dynamic PET. J Nucl Med. 2017;58(9):1471-1476. <https://doi.org/10.2967/jnumed.116.187211>. © SNMMI.)

various metabolites, ions, proteins, lipids, cytokines and chemokines, and other biomolecules in an extracellular matrix affecting cellular function. The early A β plaque pathology of AD is found in the ECS and arterial smooth muscle cells.⁹⁴ The change of the molecular contents and concentrations in the extracellular space are believed to be affected by the fluid dynamics in this space. For instance, it has been reported that the ECS enlargement during sleep could enhance the brain ISF clearance.¹¹

Extracellular fluid as a key component of glymphatic system

The extracellular fluid includes both interstitial fluid and CSF in PVS. The movement of ISF in the ECS is generally considered as diffusion dependent, whereas CSF in PVS is reported as having a faster movement speed than ISF but slower than the blood flow in adjacent vessels. The ECS volume is about 30~45% of total tissue volume measured by DTI based Free Water in which there is about

3~6% of PVS measured by MR T2-relaxation based CSF fraction.^{21,95,96} The fluid exchange between ISF and CSF in PVS is considered as the main mechanism of glymphatic function to clear brain metabolites. Therefore, the study of extracellular fluid dynamic is critical to understand the glymphatic function in the brain parenchymal. Dynamic PET could play a significant role in estimating the ISF fluid dynamic in ECS.

In 2022, Suzuki and colleagues examined interstitial flow dynamics using ^{15}O -H $_2\text{O}$ PET.²⁵ They designed a model with 2 parameters by fitting the TAC curve in LV and GM to 1-exponential with an additional constant. The ratio of fitted constant in LV and gray matter was defined as influx ratio (IR) and the fitted decay rate in GM was defined as the drain rate (DR). Their results showed that NL subjects had no significant change in IR and DR after 2 years (IR: 1.03 ± 0.21 and 1.02 ± 0.20 , DR: 1.74 ± 0.43 and 1.67 ± 0.47 , respectively), but 3 A β + subjects had decreased DR (IR: 0.60 ± 0.15 and 0.60 ± 0.13 , DR: 1.24 ± 0.12 and $1.11 \pm$

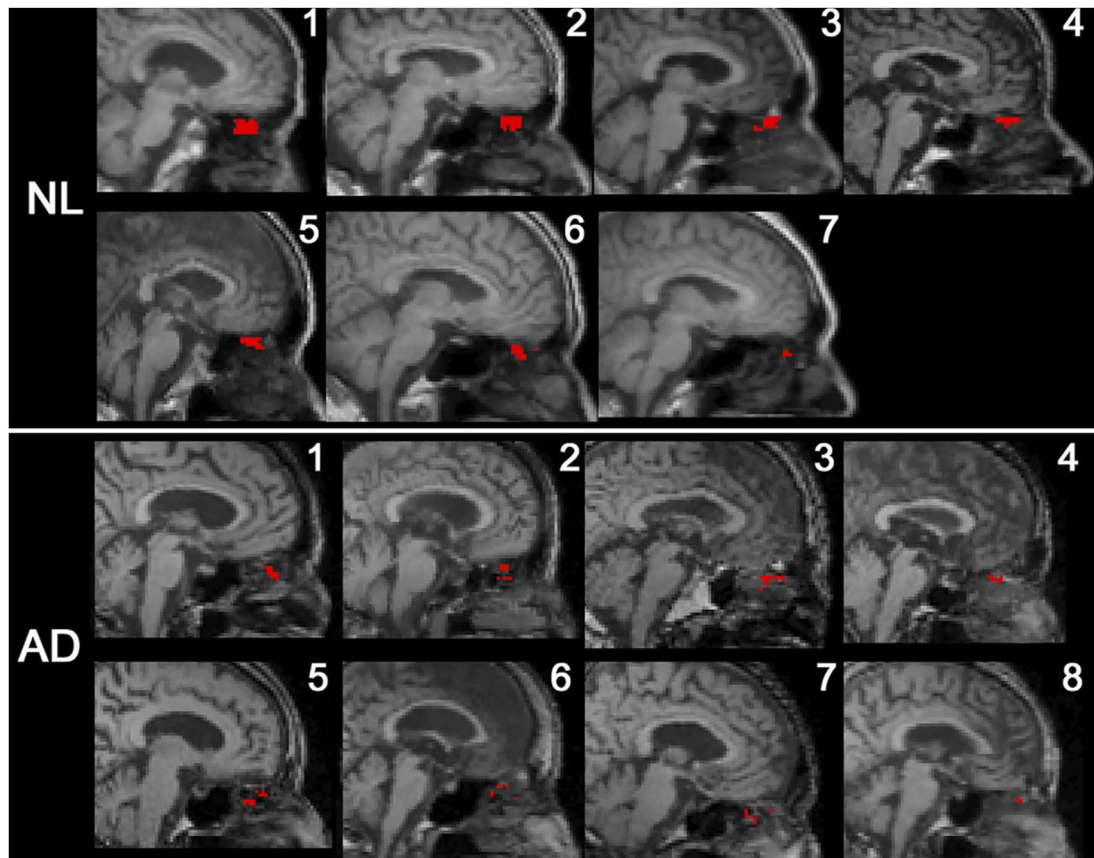


Fig. 5. Midsagittal MR image with superimposed PET data from all subjects. CSF-positive voxels falling into a superior turbinate region of interest (ROI), consistent with red colored region in Fig. 4A. (This research was originally published in JNM. de Leon MJ, Li Y, Okamura N, et al. Cerebrospinal Fluid Clearance in Alzheimer Disease Measured with Dynamic PET. *J Nucl Med.* 2017;58(9):1471-1476. <https://doi.org/10.2967/jnumed.116.187211>. © SNMMI.)

0.10). These data further suggested that progressive BCSF barrier function disturbances could be related to A β measures.

In 2024, Suzuki, and colleagues performed a normal aging and AD study using the same ^{15}O -H $_2\text{O}$ PET tracer and model. The results showed that interstitial fluid flow decreased with age, especially after 50 year old.⁸⁴ They also showed that both IR and DR for elderly NL (age: 65–79, IR: 1.04 ± 0.17 , DR: 1.45 ± 0.39) were lower than young NL (age: 35–49, IR: 1.33 ± 0.08 , DR: 1.92 ± 0.09) and higher than that for AD (age 59–84, IR: 0.74 ± 0.09 , DR: 0.86 ± 0.17), implying a decreased influx ratio and interstitial fluid drainage for elderly and AD. A significant negative linear correlation was observed between age and the 2 indices (IR: $R^2 = 0.54$ and DR: $R^2 = 0.44$). These results are in agreement with a published normal aging findings reported above using ^{11}C -Butanol tracer influx and clearance from brain.⁹² Although both ^{15}O -H $_2\text{O}$ and ^{11}C -Butanol have no noticeable tissue binding, they have very different half-lives, 2 min versus 20 min. This leads to scan acquisition

time differences and different shaped TAC curves, resulting in different input and clearance estimates. Nevertheless, at this time it is encouraging that similar general input and egress features related to brain amyloid are observed.

DISCUSSION

The production and clearance of brain proteins, and production and clearance of brain fluids has gained increasing attention following the amyloid hypothesis from Hardy and Selkoe that proposed the accumulation of A β as failed protein clearance in the absence of increased production.^{2,97,98} With demonstration of a failing glymphatic clearance in animal AD models associated with increased A β deposition,^{8,17} human CSF clearance studies were introduced. It's more than 20 years since the amyloid hypothesis was proposed and 12 years since the glymphatic system hypothesis in AD was proposed.^{8,98} The glymphatic system includes the network of PVS facilitating fluid exchanges between SAS, CSF, and the ISF from

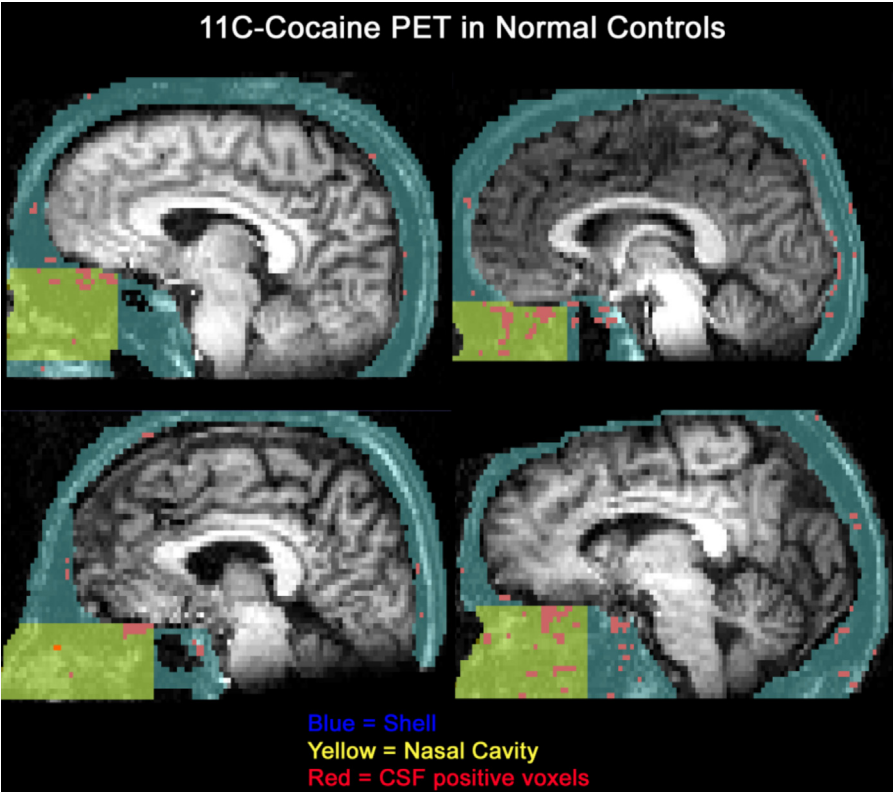


Fig. 6. Nasal turbinate signal using ^{11}C -cocaine PET data in normal young subjects. Voxels whose LV CSF correlations exceeded $r = 0.95$ were considered CSF positive and are mapped in red below. Within the blue shell region, a nasal cavity region was defined in yellow. As observed with the ^{18}F -THK-5117 tau tracer, the highest density of presumed CSF positive sites is in the superior and middle turbinate regions.^{75,89} This was obtained over 40 min following IV injection of 6 to 8 mCi of ^{11}C -cocaine. Superior and middle turbinate regions provided the highest density of CSF-correlated voxels. (Source Supplementary materials of : de Leon MJ, Li Y, Okamura N, et al. Cerebrospinal Fluid Clearance in Alzheimer Disease Measured with Dynamic PET. J Nucl Med. 2017;58(9):1471-1476. <https://doi.org/10.2967/jnumed.116.187211>.)

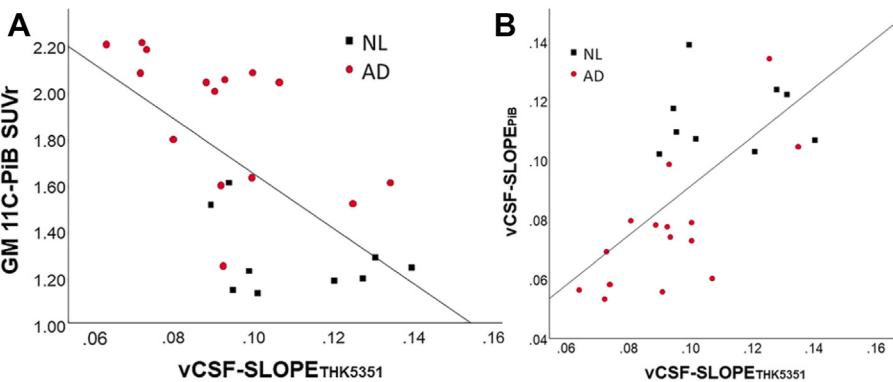


Fig. 7. The performance of vCSF of its association with amyloid deposition and across tracers' consistency. (A) The vCSF-SLOPETHK5351 is inversely correlated with the extent of fibrillar $\text{A}\beta$ as estimated by ^{11}C -PiB gray matter binding ($r = -0.64$, $P < .01$, $n = 24$). The correlation remains significant when restricted to the AD group ($r = -0.58$, $P < .05$, $n = 15$). NL: (black); AD: (red). (B) Cross-tracer agreement of clearance: the vCSF-SLOPE for ^{11}C -PiB and ^{18}F -THK5351 PET tracers are highly correlated ($r = 0.66$, $n = 24$, $P < .01$). (This research was originally published in JNM. de Leon MJ, Li Y, Okamura N, et al. Cerebrospinal Fluid Clearance in Alzheimer Disease Measured with Dynamic PET. J Nucl Med. 2017;58(9):1471-1476. <https://doi.org/10.2967/jnumed.116.187211>. © SNMMI.)

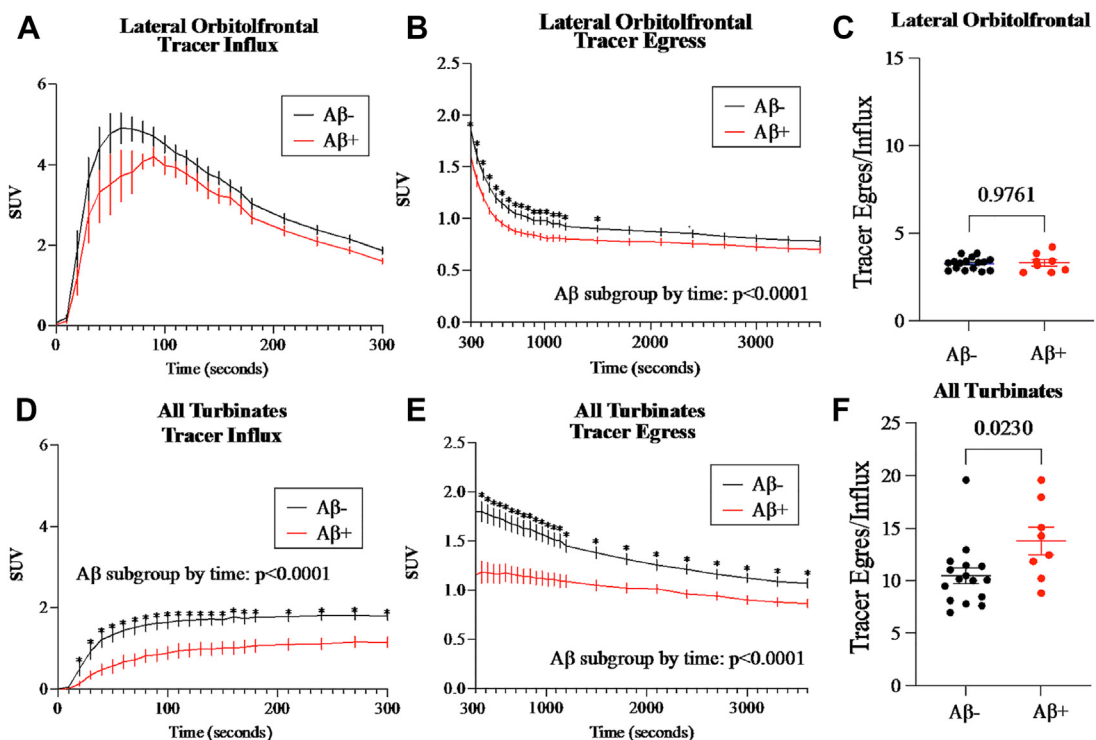


Fig. 8. PET Butanol Influx and Egress in Lateral Orbitofrontal Cortex and All-turbinates. The effect of brain amyloid positivity on PET Butanol (SUV) influx and egress for both the LOF (A–C) and All-turbinates (D–F). The regional influx TAC from 0 to 5 min is seen in (A, D) and for the egress the TAC 5 to 60 min (B, E). (A, B) Using a Repeated Measures Two-2 ANOVA, the LOF influx showed a Aβ subgroup trend ($F(1,22) = 3.16, P = .0892$), and LOF egress showed a main effect of Aβ subgroup ($F(1,22) = 4.641, P = .0424$) and Aβ subgroup by time interaction ($F(329, 7238) = 4.964, P < .0001$). (D, E). For the influx to the All-turbinates, there was a main effect of Aβ subgroup and Aβ subgroup by time interaction: ($F(1,22) = 10.24, P = .0041$ and $F(30,660) = 2.975, P < .0001$, respectively) and for the egress from the All-turbinates: ($F(1,22) = 11.36, P = .0028$ and $F(329, 7238) = 11.67, P < .0001$, respectively). To assess the relative contributions of influx on egress within LOF and All-turbinates, the egress AUC was normalized by influx AUC (C, F). Mann-Whitney assessment of the normalized egress showed for the All-turbinates a significantly higher tracer ratio in Aβ+ subjects. Aβ individuals are displayed in black, and Aβ+ in red. Error bars represent the standard error of the mean on each time frame. FDR corrected significant differences at specific timepoints are denoted by significant Aβ subgroup related influx or egress effects ($P > .05$). (Source Mehta NH, Wang X, Keil SA, et al. [1-11C]-Butanol Positron Emission Tomography reveals an impaired brain to nasal turbinates pathway in aging amyloid positive subjects. *Fluids Barriers CNS*. 2024;21(1):30. <https://doi.org/10.1186/s12987-024-00530-y>.)

the ECS. The study of microscale fluid exchange using human imaging modalities with large voxel sizes is on the one hand challenging, but on the other the expanded field of view beyond small windows offering microscopic level detection appears to offer some advantages.

The imaging of neurofluids using PET is an emerging research topic. As summarized above, both CSF and ISF in the brain have recently been studied using PET radiotracers as CSF surrogates. However, the number of published studies remains small and the anatomic and clinical features examined limited. Additional PET imaging studies are needed to evaluate the CSF and ISF dynamics from various brain sites considering both age and disease. Overall, the data consistently demonstrate CSF clearance reductions associated with age and possibly additional influx deficits associated with

amyloid lesions. At present, several anatomic CSF pathways including brain, ventricle, and olfactory regions have been examined using PET, and interestingly, both tracer input and egress deficits have been shown for amyloid positive tissues suggesting a further characterization of tissue properties such as their permeability to tracers.

The Relationship Between Brain and Nasal Turbinate Kinetics

The introduction of PET and PET tracers like ^{11}C -Butanol and ^{15}O -H $_2$ O PET offers a novel tool for *in-vivo* assessment of fluid clearance dynamics through the brain, nasal turbinates, carotid artery, internal jugular vein, and other sites. Where earlier studies depended on ventricular sampling and tau and amyloid tracers, both confounded by brain

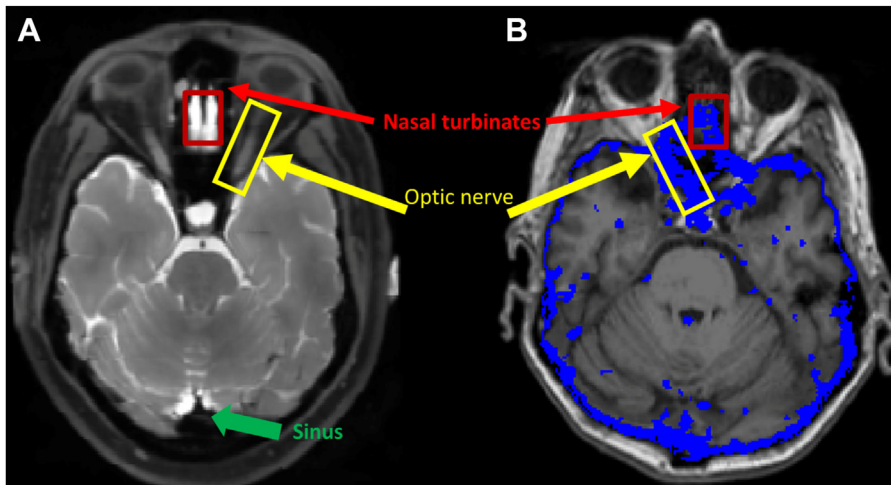


Fig. 9. An intrathecal Gd (left) based validation of ^{11}C -Butanol PET (right) CSF/ISF regions (blue). The PET CSF image was defined as the slowest CSF clearance rate by selecting the 1st quartile from the 5 to 15 mins TAC slope.⁵ It highlights the CSF distributions for 2 subjects: (A) the intrathecal injection of Gd contrast and (B) the ^{11}C -Butanol PET distribution defined as the slowest CSF clearance derived from the 1st quartile of the 5 to 15 mins TAC slope. From the images in (A), we observe many consistencies between the enhanced CSF signal following intrathecal injection of Gd contrast with the slowest quartile CSF slopes in areas marked as blue mask in (B). (Source Agarwal N, Lewis LD, Hirschler L, et al. Current Understanding of the Anatomy, Physiology, and Magnetic Resonance Imaging of Neurofluids: Update From the 2022 "ISMRM Imaging Neurofluids Study group" Workshop in Rome. J Magn Reson Imaging. 2024;59(2):431-449. <https://doi.org/10.1002/jmri.28759>).

binding, ^{11}C -Butanol and ^{15}O -H₂O PET have demonstrated value in this space. Both tracers have low molecular weights, are freely diffusible, and do not bind in brain.^{91,99} Distinguishing these tracers, ^{11}C -Butanol has a longer 20 min versus 2 min half-life.

Prior work has revealed the metabolic fate and modeling of ^{11}C -Butanol in clinical applications using ^{11}C -Butanol as a blood flow agent sampling brain for approximately 5 min.^{90,93} Capitalizing on these biophysical properties, the tracer concentration and kinetics between arterial and venous blood, brain, and nasal turbinates for 60 min was investigated. The results showed significant concentration and time-dependent changes. All the emerging modeling approaches included in the review, including vCSF, t75%, input, and clearance and tracers used are in general agreement. Caution is advised when applying tracers with either specific or non-specific binding properties, such as the ^{18}F -MK-6240 binds to tau and to bone, either of which could impact the results.

Validation of Neurofluids Quantification

The validation of human neurofluid quantification is both complex and in its infancy. Validation studies are needed for CSF and ISF distributions comparing PET imaging with the intrathecal injection of Gd measured by dynamic contrast enhancement.^{5,23} Examples of this using ^{11}C -Butanol are shown in

Figs. 9 and 10. Furthermore, validations are needed using longitudinal clinical analyses, subject challenge protocols, diverse disease populations, and animal models.

Future Considerations

As summarized above, most PET quantification modeling to date used ROI-based calculations. This approach has been useful for diagnostic signal changes between subject groups. However, the value could be improved when considering the early detection of pathologic change on an individual basis. One next step will be to extend the analyses to the voxel level to improve characterization of pathologic and functional changes. We also envision extending the CSF mapping to other cranial nerves, lymphatic structures, and to veins. Further, the modeling of fluid exchanges between tissue compartments and their interactions could be improved. As such, future directions will no doubt explore the regional and voxel level interactions between CBF, CSF, and ISF dynamics in a search for early identifiable features of future clinical risk. Finally, diverse animal models will be helpful to validate the interaction between fluid compartments and provide ground truth of the fluid dynamics in the brain.

SUMMARY

In summary, PET CSF dynamic imaging complements MR imaging based dynamic CSF imaging

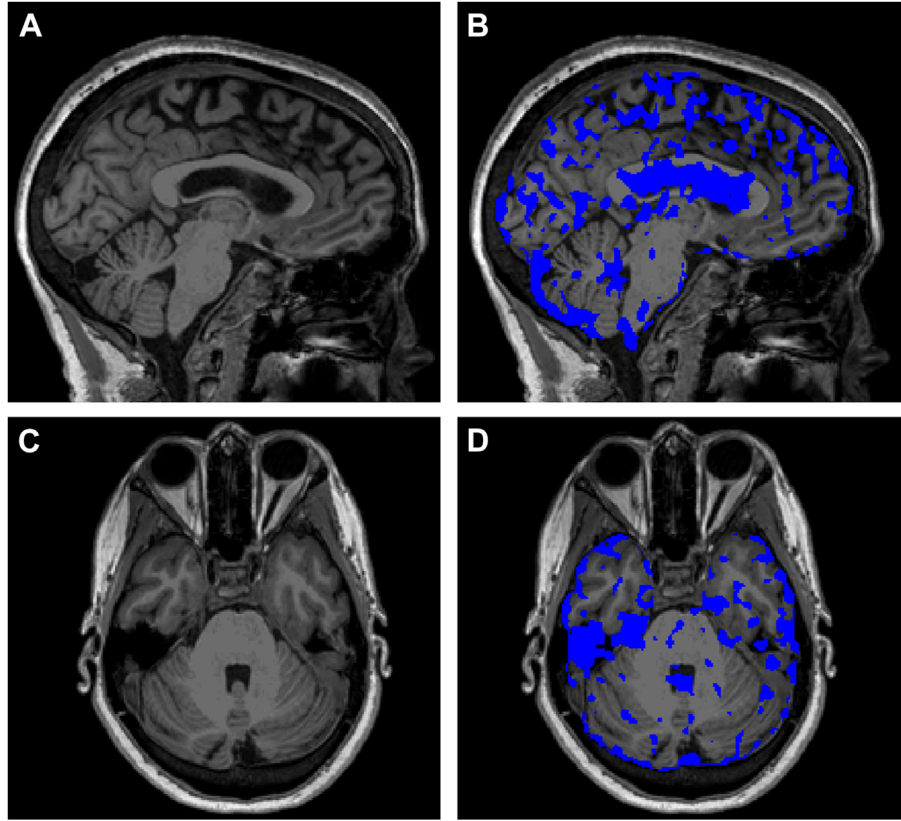


Fig. 10. An example of the 1st quartile slowest tracer clearance region defined by the slope of PET TAC during 5 min to 15 min post tracer injection of ^{11}C -Butanol tracer. (A) and (C) are the sagittal and axial view of the same brain. (B) and (D) show the same views with dynamic ^{11}C -Butanol PET defined slowest clearance region mask overlayed. This depicts another anatomic validation example from the ^{11}C -Butanol PET data. Within subject and for the whole brain, the slowest 1st quartile slope maps the sulcal and ventricular CSF but not a faster clearing ISF. (Courtesy de Leon MJ, Li Y, Zhou L.)

approaches. PET with a low-radiation dose and IV administration provides quantitative opportunities in imaging brain neurofluids. This includes whole brain (and body) coverage, tissue clearance and permeability measurements, high contrast sensitivity, and tracer half-lives permitting repeat examinations. In less than a decade, PET tracers have demonstrated a role for functional PET mapping of neurofluids, contributing to AD diagnoses, and revealing correlations with related brain pathology. The future is encouraging for expanded tissue mapping, longitudinal treatment evaluations, and mechanistic validation approaches.

CLINICS CARE POINTS

- The recent experimental studies of neurofluid quantification using PET imaging reported in this review were designed to improve the understandings of CSF clearance in aging and AD. These data support the view that CSF clearance and the formation of

amyloid lesions are closely related. Such observations may improve sensitivity for the diagnosis and progression of AD and assist in developing and monitoring therapeutic interventions.

ACKNOWLEDGMENT

We thank the Weill Cornell Medicine CBIC team, including: Drs John Babich, P. David Mozley, Simon Morin, Sadek Nehmeh, Nicholas Karakatsanis, Stefan Gohlke, Keunpoong Lim, Nicole Waterhouse, Ruth Fernandez, Besim Islami, and Eva Burnazi, for their work in the development, synthesis, and testing of ^{11}C -Butanol. We thank Xiuyuan Hugh Wang of the Weill Cornell Medicine Brain Health Imaging Institute for valuable discussions and image processing. We thank Drs Jonathan Dyke from Weill Cornell Medicine and Joseph Levi Chazen from Hospital for Special Surgery New York for their contributions to the MR imaging validations of the PET data. We are

most grateful for the critical discussions provided by Drs Gloria Chiang, Lidia Glodzik, Tracy Butler, and Samantha Keil from the Brain Health Imaging Institute, Department of Radiology, Weill Cornell Medicine.

DISCLOSURE

Research reported in this publication was supported in part by the following grants: United States National Institutes of Health/National Institute on Aging R56 AG058913 (M. de Leon), RF1 AG057570 (M. de Leon), and R01 AG057848 (Y. Li).

REFERENCES

- Delpire E. and Gagnon K.B., Chapter one - water homeostasis and cell volume maintenance and regulation, In: *Current topics in membranes. Cell volume regulation*, 2018, Vol. 81. Academic Press; San Diego, CA, 3–52.
- Tarasoff-Conway JM, Carare RO, Osorio RS, et al. Clearance systems in the brain-implications for Alzheimer disease. *Nat Rev Neurol* 2015;11(8):457–70.
- Hladky SB, Barrand MA. Mechanisms of fluid movement into, through and out of the brain: evaluation of the evidence. *Fluids Barriers CNS* 2014;11:26.
- Mestre H, Tithof J, Du T, et al. Flow of cerebrospinal fluid is driven by arterial pulsations and is reduced in hypertension. *Nat Commun* 2018;9(1):4878.
- Agarwal N, Lewis LD, Hirschler L, et al. Current understanding of the anatomy, physiology, and magnetic resonance imaging of neurofluids: update from the 2022 “ISMRM imaging neurofluids study group” Workshop in Rome. *J Magn Reson Imaging* 2024;59(2):431–49.
- Iliff JJ, Lee H, Yu M, et al. Brain-wide pathway for waste clearance captured by contrast-enhanced MRI. *J Clin Invest* 2013;123(3):1299–309.
- Kaur J, Fahmy LM, Davoodi-Bojd E, et al. Waste clearance in the brain. *Front Neuroanat* 2021;15:665803.
- Iliff JJ, Wang M, Liao Y, et al. A paravascular pathway facilitates CSF flow through the brain parenchyma and the clearance of interstitial solutes, including amyloid β . *Sci Transl Med* 2012;4(147):147ra111.
- Iliff JJ, Wang M, Zeppenfeld DM, et al. Cerebral arterial pulsation drives paravascular CSF–interstitial fluid exchange in the Murine brain. *J Neurosci* 2013;33(46):18190–9.
- Rasmussen MK, Mestre H, Nedergaard M. The glymphatic pathway in neurological disorders. *Lancet Neurol* 2018;17(11):1016–24.
- Xie L, Kang H, Xu Q, et al. Sleep drives metabolite clearance from the adult brain. *Science* 2013;342(6156):373–7.
- Fultz NE, Bonmassar G, Setsompop K, et al. Coupled electrophysiological, hemodynamic, and cerebrospinal fluid oscillations in human sleep. *Science* 2019;366(6465):628–31.
- Hablit LM, Nedergaard M. The glymphatic system: a novel component of fundamental neurobiology. *J Neurosci* 2021;41(37):7698–711.
- Benveniste H, Liu X, Koundal S, et al. The glymphatic system and waste clearance with brain aging: a review. *Gerontology* 2019;65(2):106–19.
- Rodrigue KM, Rieck JR, Kennedy KM, et al. Risk factors for β -amyloid deposition in healthy aging. *JAMA Neurol* 2013;70(5):600–6.
- Okamura N, Yanai K. Florbetapir (18F), a PET imaging agent that binds to amyloid plaques for the potential detection of Alzheimer's disease. *IDrugs Investig Drugs J*. 2010;13(12):890–9.
- Mawuenyega KG, Sigurdson W, Ovod V, et al. Decreased clearance of CNS β -amyloid in Alzheimer's disease. *Science* 2010;330(6012):1774.
- Wen Q, Tong Y, Zhou X, et al. Assessing pulsatile waveforms of paravascular cerebrospinal fluid dynamics using dynamic diffusion-weighted imaging (dDWI). *Neuroimage* 2022;260:119464.
- Taoka T, Masutani Y, Kawai H, et al. Evaluation of glymphatic system activity with the diffusion MR technique: diffusion tensor image analysis along the perivascular space (DTI-ALPS) in Alzheimer's disease cases. *Jpn J Radiol* 2017;35(4):172–8.
- Zhou L, Butler TA, Wang XH, et al. Multimodal assessment of brain fluid clearance is associated with amyloid-beta deposition in humans. *J Neuroradiol* 2023. <https://doi.org/10.1016/j.neurad.2023.10.009>.
- Zhou L, Nguyen TD, Chiang GC, et al. Parenchymal CSF fraction is a measure of brain glymphatic clearance and positively associated with amyloid beta deposition on PET. *Alzheimers Dement* 2024;20(3):2047–57.
- Ford JN, Zhang Q, Sweeney EM, et al. Quantitative water permeability mapping of blood-brain-barrier Dysfunction in aging. *Front Aging Neurosci* 2022;14:867452.
- Eide PK, Lashkarivand A, Hagen-Kersten ÅA, et al. Intrathecal contrast-enhanced magnetic resonance imaging of cerebrospinal fluid dynamics and glymphatic enhancement in Idiopathic normal pressure Hydrocephalus. *Front Neurol* 2022;13. <https://doi.org/10.3389/fneur.2022.857328>.
- Schubert JJ, Veronese M, Marchitelli L, et al. Dynamic ^{11}C -PiB PET shows cerebrospinal fluid flow alterations in Alzheimer disease and multiple sclerosis. *J Nucl Med* 2019;60(10):1452–60.
- Suzuki Y, Nakamura Y, Igarashi H. Blood cerebrospinal fluid barrier function disturbance can be followed by amyloid- β accumulation. *J Clin Med* 2022;11(20):6118.

26. Bonte FJ. Nuclear Medicine Pioneer Citation, 1976: David E. Kuhl, M.D. *J Nucl Med* 1976;17(6):518–9.
27. Reivich M, Kuhl D, Wolf A, et al. The [^{18}F]fluorodeoxyglucose method for the measurement of local cerebral glucose utilization in man. *Circ Res* 1979; 44(1):127–37.
28. Croll MN. Nuclear medicine instrumentation. Historic perspective. *Semin Nucl Med* 1994;24(1):3–10.
29. Reivich M, Alavi A, Wolf A, et al. Glucose metabolic rate kinetic model parameter determination in humans: the Lumped constants and rate constants for [^{18}F]fluorodeoxyglucose and [^{11}C]deoxyglucose. *J Cereb Blood Flow Metab* 1985; 5(2):179–92.
30. Hartvig P, Lindner KJ, Tedroff J, et al. Regional brain kinetics of 6-fluoro-(β - ^{11}C)-L-dopa and (β - ^{11}C)-L-dopa following COMT inhibition. A study in vivo using positron emission tomography. *J Neural Transm Gen Sect JNT* 1992;87(1):15–22.
31. Kanno I, Takahashi M, Yamaya T, et al. 1925–1996): a pioneer of positron emission tomography weighted in fast imaging and Oxygen-15 application. *Radiol Phys Technol* 2020;13(1):1–5.
32. Phelps ME. PET: the merging of biology and imaging into molecular imaging. *J Nucl Med* 2000;41(4): 661–81.
33. Phelps ME. Positron emission tomography provides molecular imaging of biological processes. *Proc Natl Acad Sci* 2000;97(16):9226–33.
34. Ter-Pogossian MM, Herscovitch P. Radioactive oxygen-15 in the study of cerebral blood flow, blood volume, and oxygen metabolism. *Semin Nucl Med* 1985;15(4):377–94.
35. Cherry SR, Jones T, Karp JS, et al. Total-body PET: maximizing sensitivity to create new opportunities for clinical research and patient care. *J Nucl Med* 2018;59(1):3–12.
36. Vandenberghe S, Moskal P, Karp JS. State of the art in total body PET. *EJNMMI Phys* 2020;7(1):35.
37. Zhang X, Cherry SR, Xie Z, et al. Subsecond total-body imaging using ultrasensitive positron emission tomography. *Proc Natl Acad Sci U S A* 2020;117(5): 2265–7.
38. Bao W, Xie F, Zuo C, et al. PET neuroimaging of Alzheimer's disease: radiotracers and their utility in clinical research. *Front Aging Neurosci* 2021;13: 624330.
39. Ferris SH, de Leon MJ, Wolf AP, et al. Positron emission tomography in the study of aging and senile dementia. *Neurobiol Aging* 1980;1(2):127–31.
40. de Leon MJ, Ferris SH, George AE, et al. Positron emission tomographic studies of aging and Alzheimer disease. *AJNR Am J Neuroradiol* 1983;4(3): 568–71.
41. de Leon MJ, Convit A, Wolf OT, et al. Prediction of cognitive decline in normal elderly subjects with 2-[(^{18}F)]fluoro-2-deoxy-D-glucose/positron-emission tomography (FDG/PET). *Proc Natl Acad Sci U S A*. 2001;98(19):10966–71.
42. Friedland RP, Jagust WJ, Huesman RH, et al. Regional cerebral glucose transport and utilization in Alzheimer's disease. *Neurology* 1989;39(11):1427–34.
43. Friedland RP, Brun A, Budinger TF. Pathological and positron emission tomographic correlations in Alzheimer's disease. *Lancet Lond Engl* 1985;1(8422): 228.
44. Mosconi L, Tsui WH, De Santi S, et al. Reduced hippocampal metabolism in MCI and AD: automated FDG-PET image analysis. *Neurology* 2005;64(11): 1860–7.
45. Bobinski M, de Leon MJ, Wegiel J, et al. The histological validation of post mortem magnetic resonance imaging-determined hippocampal volume in Alzheimer's disease. *Neuroscience* 2000;95(3): 721–5.
46. Gómez-Isla T, Hollister R, West H, et al. Neuronal loss correlates with but exceeds neurofibrillary tangles in Alzheimer's disease. *Ann Neurol* 1997;41(1):17–24.
47. Mosconi L, Berti V, Glodzik L, et al. Pre-clinical detection of Alzheimer's disease using FDG-PET, with or without amyloid imaging. *J Alzheimers Dis JAD* 2010;20(3):843–54.
48. Tripathi M, Tripathi M, Damle N, et al. Differential diagnosis of neurodegenerative dementias using metabolic phenotypes on F-18 FDG PET/CT. *Neuro-Radiol J* 2014;27(1):13–21.
49. Wong KP, Wardak M, Shao W, et al. Quantitative analysis of [^{18}F]FDDNP PET using subcortical white matter as reference region. *Eur J Nucl Med Mol Imaging* 2010;37(3):575–88.
50. Klunk WE, Engler H, Nordberg A, et al. Imaging brain amyloid in Alzheimer's disease with Pittsburgh Compound-B. *Ann Neurol* 2004;55(3):306–19.
51. Lopresti BJ, Klunk WE, Mathis CA, et al. Simplified quantification of Pittsburgh Compound B amyloid imaging PET studies: a comparative analysis. *J Nucl Med* 2005;46(12):1959–72.
52. Mathis CA, Mason NS, Lopresti BJ, et al. Development of positron emission tomography β -amyloid plaque imaging agents. *Semin Nucl Med* 2012; 42(6):423–32.
53. Martínez G, Vernooij RW, Fuentes Padilla P, et al. ^{18}F PET with flutemetamol for the early diagnosis of Alzheimer's disease dementia and other dementias in people with mild cognitive impairment (MCI). *Cochrane Database Syst Rev* 2017;2017(11):CD012884.
54. Villemagne VL, Ong K, Mulligan RS, et al. Amyloid imaging with ^{18}F -Florbetaben in Alzheimer disease and other dementias. *J Nucl Med* 2011;52(8):1210–7.
55. Barthel H. First tau PET tracer approved: toward Accurate in vivo diagnosis of Alzheimer disease. *J Nucl Med* 2020;61(10):1409–10.
56. Hostetler ED, Walji AM, Zeng Z, et al. Preclinical characterization of ^{18}F -MK-6240, a Promising PET

- tracer for in vivo quantification of human neurofibrillary tangles. *J Nucl Med* 2016;57(10):1599–606.
57. Mueller A, Bullich S, Barret O, et al. Tau PET imaging with 18F-PI-2620 in patients with alzheimer disease and healthy controls: a first-in-humans study. *J Nucl Med* 2020;61(6):911–9.
 58. Imaizumi M, Kim HJ, Zoghbi SS, et al. PET imaging with [11C]PBR28 can localize and quantify upregulated peripheral benzodiazepine receptors associated with cerebral ischemia in rat. *Neurosci Lett* 2007;411(3):200–5.
 59. Pike VW, Halldin C, Crouzel C, et al. Radioligands for PET studies of central benzodiazepine receptors and PK (peripheral benzodiazepine) binding sites—current status. *Nucl Med Biol* 1993;20(4):503–25.
 60. Kumar A, Koistinen NA, Malarte ML, et al. Astroglial tracer BU99008 detects multiple binding sites in Alzheimer's disease brain. *Mol Psychiatry* 2021;26(10):5833–47.
 61. Nakamura Y, Suzuki Y, Tsujita M, et al. Development of a novel ligand, [11C]TGN-020, for aquaporin 4 positron emission tomography imaging. *ACS Chem Neurosci* 2011;2(10):568–71.
 62. Smith R, Capotosti F, Schain M, et al. The α -synuclein PET tracer [18F] ACI-12589 distinguishes multiple system atrophy from other neurodegenerative diseases. *Nat Commun* 2023;14(1):6750.
 63. Cross DJ, Mosci K, Minoshima S. In: *Molecular imaging of Neurodegenerative disorders*. Cham, Switzerland: Springer International Publishing; 2023. <https://doi.org/10.1007/978-3-031-35098-6>.
 64. Nasrallah I, Dubroff J. An overview of PET neuroimaging. *Semin Nucl Med* 2013;43(6):449–61.
 65. Shukla AK, Kumar U. Positron emission tomography: an overview. *J Med Phys Assoc Med Phys India* 2006;31(1):13–21.
 66. Macedo AC, Tissot C, Therriault J, et al. The Use of tau PET to stage Alzheimer disease According to the Braak staging Framework. *J Nucl Med* 2023;64(8):1171–8.
 67. Therriault J, Zimmer ER, Benedet AL, et al. Staging of Alzheimer's disease: past, present, and future perspectives. *Trends Mol Med* 2022;28(9):726–41.
 68. Prince MR, Zhang H, Zou Z, et al. Incidence of immediate gadolinium contrast media reactions. *AJR Am J Roentgenol* 2011;196(2):W138–43.
 69. Eide PK, Ringstad G. MRI with intrathecal MRI gadolinium contrast medium administration: a possible method to assess glymphatic function in human brain. *Acta Radiol Open* 2015;4(11):2058460115609635.
 70. Rane LS, Flores J, Peskind ER, et al. Preliminary investigations into human neurofluid transport using multiple novel non-contrast MRI methods. *J Cereb Blood Flow Metab* 20240271678X241264407. <https://doi.org/10.1177/0271678X241264407>.
 71. Alsop DC, Detre JA, Golay X, et al. Recommended Implementation of arterial spin labeled perfusion MRI for clinical applications: a consensus of the ISMRM perfusion study group and the European Consortium for ASL in dementia. *Magn Reson Med* 2015;73(1):102–16.
 72. Zhou L, Zhang Q, Spincemaille P, et al. Quantitative transport mapping (QTM) of the kidney with an approximate microvascular network. *Magn Reson Med* 2021;85(4):2247–62.
 73. Guo Y, Zhou L, Li Y, et al. Quantitative transport mapping of multi-delay arterial spin labeling MRI detects early blood perfusion alterations in Alzheimer's disease. *Alzheimer's Res Ther* 2024;16(1):156.
 74. Wang DJ, Hua J, Cao D, et al. Neurofluids and the glymphatic system: anatomy, physiology, and imaging. *Br J Radiol* 2023;96(1151):20230016.
 75. de Leon MJ, Li Y, Okamura N, et al. Cerebrospinal fluid clearance in Alzheimer disease measured with dynamic PET. *J Nucl Med* 2017;58(9):1471–6.
 76. Li Y, Rusinek H, Butler T, et al. Decreased CSF clearance and increased brain amyloid in Alzheimer's disease. *Fluids Barriers CNS* 2022;19(1):21.
 77. Herscovitch P, Raichle ME, Kilbourn MR, et al. Positron emission tomographic measurement of cerebral blood flow and permeability-surface area product of water using [15O]water and [11C]butanol. *J Cereb Blood Flow Metab* 1987;7(5):527–42.
 78. Logan J, Fowler JS, Volkow ND, et al. Graphical analysis of reversible radioligand binding from time-activity measurements applied to [N-11C-methyl]-(-)-cocaine PET studies in human subjects. *J Cereb Blood Flow Metab* 1990;10(5):740–7.
 79. Benveniste H, Lee H, Ozturk B, et al. Glymphatic cerebrospinal fluid and Solute transport quantified by MRI and PET imaging. *Neuroscience* 2021;474:63–79.
 80. Patlak CS, Blasberg RG, Fenstermacher JD. Graphical evaluation of blood-to-brain transfer constants from multiple-time uptake data. *J Cereb Blood Flow Metab* 1983;3(1):1–7.
 81. Carson RE. Tracer kinetic modeling in PET. In: *Positron emission tomography: basic sciences*. Singapore: Springer; 2005. p. 127–59. https://doi.org/10.1007/1-84628-007-9_6.
 82. Bentourkia M, Zaidi H. Tracer kinetic modeling in nuclear medicine: theory and applications. In: Zaidi H, editor. *Quantitative analysis in nuclear medicine imaging*. Singapore: Springer; 2006. p. 391–413.
 83. Logan J, Fowler JS, Volkow ND, et al. Distribution volume ratios without blood sampling from graphical analysis of PET data. *J Cereb Blood Flow Metab* 1996;16(5):834–40.
 84. Suzuki Y, Nakamura Y, Igarashi H. Interstitial fluid flow decreases with age, especially after 50 years. *Neurobiol Aging* 2024. <https://doi.org/10.1016/j.neurobiolaging.2024.05.006>.

85. Fujii N, Nomura S, Izuma H, et al. Which theory of cerebrospinal fluid production and Absorption do Neurosurgeons Teach to Medical Students? Survey from Medical Universities in Japan, 2022. *Neurol Med -Chir* 2024;64(6):241–6.
86. Kelley DH, Thomas JH. Cerebrospinal fluid flow. *Annu Rev Fluid Mech* 2023;55(Volume 55, 2023): 237–64.
87. Silver I, Kim C, Mollanji R, et al. Cerebrospinal fluid outflow resistance in sheep: impact of blocking cerebrospinal fluid transport through the cribriform plate. *Neuropathol Appl Neurobiol* 2002;28(1):67–74.
88. Johnston M, Zakharov A, Koh L, et al. Subarachnoid injection of Microfil reveals connections between cerebrospinal fluid and nasal lymphatics in the non-human primate. *Neuropathol Appl Neurobiol* 2005; 31(6):632–40.
89. Mehta NH, Sherbansky J, Kamer AR, et al. The brain-nose Interface: a potential cerebrospinal fluid clearance site in humans. *Front Physiol* 2022;12. <https://doi.org/10.3389/fphys.2021.769948>.
90. Li EJ, López JE, Spencer BA, et al. Total-body perfusion imaging with [11C]-Butanol. *J Nucl Med* 2023; 64(11):1831–8.
91. Knapp WH, Helus F, Oberdorfer F, et al. 11C-butanol for imaging of the blood-flow distribution in tumor-bearing animals. *Eur J Nucl Med* 1985;10(11–12): 540–8.
92. Mehta NH, Wang X, Keil SA, et al. [1-11C]-Butanol Positron Emission Tomography reveals an impaired brain to nasal turbinates pathway in aging amyloid positive subjects. *Fluids Barriers CNS* 2024;21(1):30.
93. Votaw JR, Henry TR, Shoup TM, et al. Butanol is superior to water for performing positron emission tomography activation studies. *J Cereb Blood Flow Metab* 1999;19(9):982–9.
94. Weller RO, Preston SD, Subash M, et al. Cerebral amyloid angiopathy in the aetiology and immunotherapy of Alzheimer disease. *Alzheimer's Res Ther* 2009; 1(2):6.
95. Pasternak O, Sochen N, Gur Y, et al. Free water elimination and mapping from diffusion MRI. *Magn Reson Med* 2009;62(3):717–30.
96. Zhou L, Li Y, Sweeney EM, et al. Association of brain tissue cerebrospinal fluid fraction with age in healthy cognitively normal adults. *Front Aging Neurosci* 2023; 15:1162001.
97. Hardy J, Selkoe DJ. The amyloid hypothesis of Alzheimer's disease: progress and problems on the road to therapeutics. *Science* 2002;297(5580):353–6.
98. Selkoe DJ, Hardy J. The amyloid hypothesis of Alzheimer's disease at 25 years. *EMBO Mol Med* 2016;8(6):595–608.
99. Waterhouse NN, Kothari PJ, Dooley M, et al. Synthesis of [1–11C]Butanol via a facile solid phase extraction protocol. *Appl Radiat Isot* 2020;159:109078.